Injectable hydrogels based on silk fibroin peptide grafted hydroxypropyl chitosan and oxidized microcrystalline cellulose for scarless wound healing

Shuang Liu[a,#], Yingsong Zhao[d,#], Haojie Wei[a,#], Lei Nie[b,*], Peng Ding[b], Huixuan Sun[a], Yuandong Guo[a], Tiantian Chen[a], Oseweuba Valentine Okoro[c], Amin Shavandi[c,*], and Lihong Fan[a,*]

[a] School of Resources and Environmental Engineering, Wuhan University of Technology, Wuhan 430070, P. R. China

[b] College of Life Sciences, Xinyang Normal University, Xinyang 464000, P. R. China.

[c] BioMatter unit - École polytechnique de Bruxelles, Université Libre de Bruxelles, Avenue F.D. Roosevelt, 50 - CP 165/61, 1050 Brussels, Belgium.

[d] Department of Orthopaedics, Liyuan Hospital, Tongji Medical College, Huazhong University of Science and Technology (HUST), Wuhan 430077, P. R. China

[#]These authors contributed equally to this work and should be considered co-first authors.

Corresponding Authors

Prof. Lihong Fan:

Post address: School of Resources and Environmental Engineering, Wuhan University of Technology, 122 Luoshi Road, Wuhan, Hubei, 430070, China.

ORCID: 0000-0001-8277-4007. Tel: +86-13018011218

E-mail: lihongfan2000@hotmail.com

Prof. Lei Nie:

Post address: College of Life Sciences, Xinyang Normal University (XYNU), Xinyang

464000, China. Tel: +86-13600621068.

ORCID: 0000-0002-6175-5883

E-mail address: nieleifu@yahoo.com; nielei@xynu.edu.cn

Prof. Amin Shavandi

Post address: BioMatter unit - École polytechnique de Bruxelles, Université Libre de

Bruxelles, Avenue F.D. Roosevelt, 50 - CP 165/61, 1050 Brussels, Belgium

E-mail address: amin.shavandi@ulb.be

Abstract

Scars are consequences of the wound healing process, and eliminating scar formation remains a significant challenge. Here, an injectable HMSC hydrogel was developed based on silk fibroin peptide grafted hydroxypropyl chitosan (HPCS-*g*-SFP) and oxidized microcrystalline cellulose (OMCC) via Schiff base bonds. The synthesized HPCS-*g*-SFP copolymer displayed efficient free radical scavenging ability on hydrogen hydroxyl radicals and 1,1-diphenyl-2-picrylhydrazyl radicals (DPPH). The pore size, gelling time, equilibrium swelling rate and water retention properties of HMSC hydrogel could be regulated by changing ratio of OMCC and HPCS-*g*-SFP. Then, tetramethylpyrazine (TMP) was encapsulated into HMSC hydrogel to obtain TMP-loaded HMSC hydrogel. The TMP-loaded HMSC hydrogel facilitated 95% cell activity retention after culturing with human skin fibroblasts (HSF) or human hypertrophic scar fibroblast (HSFB) cells for 24h. Additionally, *in vivo* animal experiments confirmed that TMP-loaded HMSC hydrogel promoted rapid wound healing while preventing scar formation. The designed injectable TMP-loaded HMSC hydrogel has potentials in promoting scarless wound healing.

Keywords: hydroxypropyl chitosan, silk fibroin peptide, tetramethylpyrazine, wound healing.

1. Introduction

Wound healing is the skin tissue regeneration process involving granulation tissue and scar tissue [1]. Hydrogels are generally considered potential applications in wound healing due to their favourable biocompatibility, moisture absorption, moisture retention, and flexibility [2-5]. The applicability of hydrogel in wound healing has been extensively discussed in the literature [6-11]. For instance, Mingmao et al., [7] utilized the aminated gelatin, adipic acid hydrazide and oxidized dextran to prepare an injectable hydrogel that was loaded with β-FGF@PLGA microspheres and chlorhexidine acetate. The fabricated hydrogel could facilitate a steady release of chlorhexidine acetate and β-FGF for antibacterial effects, thus promoting wound healing. In another study, a hydrogel of 5-hydroxymethyl furfural/polyvinyl alcohol/sodium alginate hydrogel was prepared, and its wound healing properties were investigated [8]. *In vitro* investigations showed that the hydrogel could promote fibroblasts' adhesion, growth, and proliferation. Additional *in vivo* investigations established the wound healing properties of the hydrogel since it was shown to be able to reduce inflammation, promote vascular regeneration, collagen production and re-epithelialization. In another study, Hui at al., [12] developed a new hydrogel composed of collagen/oxidized microcrystalline cellulose (collagen/OMCC), demonstrating its hemostatic effect. In our previous works[13, 14], the quaternary ammonium chitosan (QCS) was modified with silk fibroin peptide (SFP), and the prepared copolymer (QCS-SFP) displayed excellent antioxidant activity, including the scavenging activity of 2,2-diphenyl-1-picrylhydrazyl (DPPH) radical, hydroxyl radical, and hydrogen peroxide.

We also grafted the collagen peptide (COP) on carboxymethyl chitosan sulfate (CMCS) using the microbial transglutaminase (MTGase) as a catalyst, the obtained polymer (CMCS-COP) showed excellent antioxidant effects without cytotoxicity against NIH-3T3 mouse fibroblasts.

Crucially, while existing hydrogels facilitate wound healing, the challenge of achieving scarless wound healing still remains. Scarless wound healing is essential since scars affect skin appearance and may also cause physical and psychological concern to some patients, thus negatively influencing the quality of life [15]. In some cases, the scar may be considered a fibroproliferative disease caused by abnormal wound healing [16]. Scarring may occur when the inflammatory phase of the wound is extended, leading to excessive proliferation of fibroblasts [17]. It was also reported that scarring might be exacerbated by reduced delivery of anti-inflammatory agents such as cytokines, nutrients and oxygen to the wound site leading to increased cell apoptosis[18]. The current medical approaches for managing scarring are divided into treatment and prevention methods [19]. The main scar prevention methods include tension-free sutures, flavonoids and pressure therapy [20-22]. The tension-free suture serves to induce rapid epithelialization of the wound site and thus prevent the formation of scars[23]. Alternatively, flavonoids and pressure therapy are based on flavonoids' functionality to inhibit the expression of SMAD2, SMAD3 and SMAD4 due to matrix metalloproteinase-1 (MMP-1) induction, leading to favourable anti-fibrotic effects for scar suppression [24, 25].

On the other hand, there is limited research into the treatment of scars, with current

studies focusing on the use of growth factors and drugs that reduce inflammation and limit scar tissue formation [26, 27]. In an attempt to provide a new approach to scarless wound treating, the current study sought to develop a tetramethylpyrazine (TMP) based hydrogel that could limit scar tissue formation. TMP is an alkaloid that can be extracted from the traditional Chinese medicine of Rhizoma Chuanxiong (Ligusticum chuanxiong Hort) [28, 29]. TMP exerts therapeutic benefits such as anti-oxidation effects and can inhibit platelet aggregation and inflammation [30, 31]. It also possesses anticoagulation and anti-fibrosis characteristics that may improve microcirculation in the wound site[30, 31]. TMP can reduce the production of reactive oxygen species and the phosphorylation of extracellular signal-regulated kinases, thus reducing the activity of activator protein [32]. Reduction in activator protein activity could inhibit the expression of vascular endothelin, leading to blood vessel expansion[32]. TMP could also inhibit the decomposition of phosphoinositide and the formation of thromboxane A_2, thus increasing nitric oxide synthase activity for inhibition of platelet aggregation and thrombus formation[33].

Due to the aforementioned properties of TMP, the current study seeks to fabricate a novel injectable hydrogel and assess the scarless wound healing potential. The TMP-loaded HSMC hydrogel was synthesized using silk fibroin peptide grafted hydroxypropyl chitosan (HPCS-g-SFP) and oxidized microcrystalline cellulose (OMCC) via the Schiff base reaction, and TMP was then in situ encapsulated to obtain TMP-loaded HSMC hydrogel, as shown in **Scheme 1**. Fourier infrared spectroscopy (FT-IR), X-ray diffraction (XRD), Scanning Electron Microscope (SEM), equilibrium

swelling rate (ESR), and water evaporation rate (WER) were used to investigate the structure and performance of the prepared hydrogels to satisfy the requirements of wound excipients. *In vitro* cell experiments explore HSMC hydrogel's cytocompatibility and TMP-loaded hydrogel on human skin fibroblasts (HSF) and hyperplastic scar fibroblasts (HSFB) were undertaken. Finally, *in vivo* animal experiments investigating the wound healing potential of injectable TMP-loaded hydrogel was undertaken.
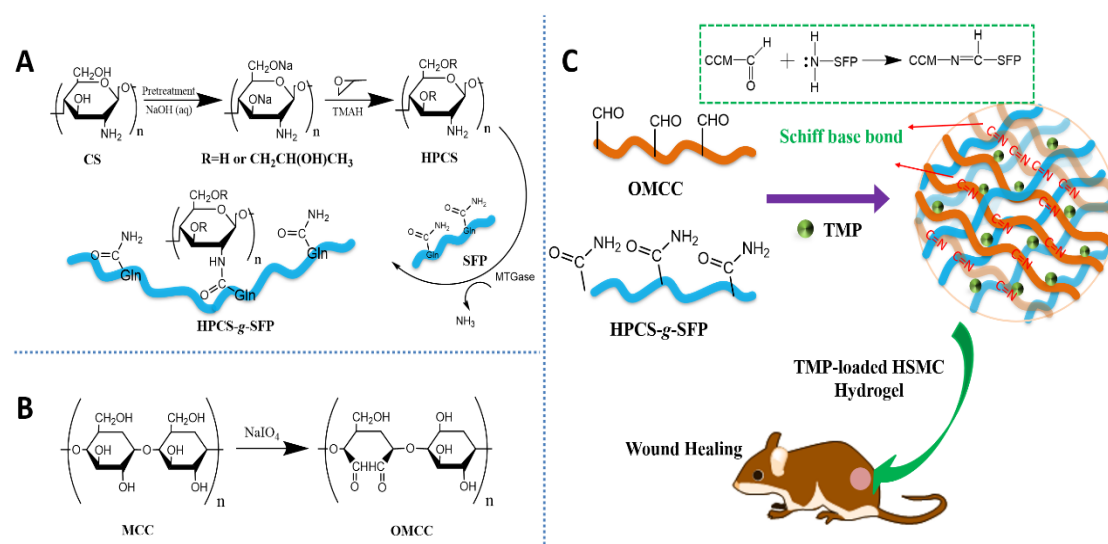
Scheme 1. The injectable TMP-loaded HSMC hydrogel was formed using silk fibroin peptide grafted hydroxypropyl chitosan (HPCS-*g*-SFP) and oxidized microcrystalline cellulose (OMCC) for wound healing application. A) The synthetic scheme of HPCS-*g*-SFP polymer; B) the synthetic scheme of OMCC polymer, C) the fabrication of TMP-loaded HSMC hydrogel via Schiff base reaction, and the hydrogels could be injected at the wound site for wound healing application.

2. Materials and Methods

2.1 Materials

In this paper, chitosan was purchased from Zhejiang Pharmaceutical gold shell Co., Ltd. Propylene oxide (C_3H_6O), tetramethylammonium hydroxide pentahydrate ($C_4H_{23}NO_6$), isopropyl alcohol (C_3H_8O), tetramethylpyrazine (TMP), and microcrystalline cellulose (MCC) were obtained from Sinopharm Chemical Reagent Co., Ltd. Microbial transglutaminase (MTGase) and silk fibroin peptide (M_w 1500) was purchased from Huashun Biological Technology Co., Ltd., Wuhan, China, without further purification. Hydroxylamine hydrochloride was obtained from Sigma-Aldrich Co., Ltd. All chemical reagents were used as received.

2.2 Synthesis of silk fibroin peptide grafted hydroxypropyl chitosan (SFP-*g*-HPCS) copolymer

Hydroxypropyl chitosan (HPCS) was synthesized according to the previous report [34]. Briefly, 10 g of alkalized chitosan and 0.8 mL of 25% tetramethylammonium hydroxide were added to 100 mL of C_3H_8O to form a homogeneous solution by mechanical stirring (1500 rpm) for 2 h, then 100 mL of propylene oxide was added to the solution at 50 °C and stirred for 4 h. After the reaction, the product was washed with ethanol thrice and subsequently dialyzed (12-14 kDa) using deionized water for 3 d, during which the water was changed every 8 h. The dialyzed solution was freeze-dried to obtain HPCS powder. To prepare HPCS-g-SFP, 1g of silk fibroin peptide (SFP) and 1 g of HPCS were dissolved in 100 mL phosphate buffer solution (PBS) to form a homogeneous solution, then 0.2 g of transglutaminase was added to the solution using

magnetic stirring (1000 rpm) for 2 h. The solution was then heated at 100 °C for 10 min. After that, the reaction solution was cooled to room temperature, circulated and subsequently dialyzed (50 kDa) against deionized water for 3 d, and the product was freeze-dried to obtain HPCS-*g*-SFP polymer powder [35]. Here, the SFP substitution ratios of HPCS-*g*-SFP copolymer were manipulated by adjusting temperature (30 °C, 40 °C, 50 °C, 60 °C, and 70 °C), reaction time (1 h, 2 h, 3 h, 4 h, and 5 h) and mass feed ratios (g/g) of SFP/HPCS (0.8, 1.0, 1.2, 1.4, and 1.6).

2.3 Synthesis of oxidized microcrystalline cellulose (OMCC) polymer

The oxidized microcrystalline cellulose polymer was prepared according to the previous literature [36]. Briefly, 5 g of microcrystalline cellulose (MCC) and 15 g of $NaIO_4$ were added to 100 mL of distilled water, and the pH of the solution was maintained to 6.8-7.2 using acetic acid. The solution was then heated at the temperature of 50 °C for 4 h, after which 100 mL of ethylene glycol was added to stop the reaction. The product was then washed with deionized water till the wash water had a pH of 7 and subsequently freeze-dried to obtain OMCC powder.

2.4 Fabrication of TMP-loaded HSMC hydrogel

To prepare the HSMC hydrogel, 1.0 g of HPCS-g-SFP polymer was dissolved in 10 mL of deionized water to obtain a uniform solution and a suspension of OMCC in distilled water with a concentration of 0.1 mg/mL was added. The resulting mixture was stored for 24 h at 25 °C to facilitate HSMC hydrogel formation. In this study, different HSMC hydrogels were prepared by using different weight feed ratios of OMCC and HPCS-*g*-SFP (1.0/1.0, 1.5/1.0, 2.0/1.0, 2.5/1.0, and 3.0/1.0), and designated as HSMC-

1, HSMC-2, HSMC-3, HSMC-4 and HSMC-5, respectively. The HSMC with the best physicochemical properties and biocompatibility, was subsequently employed in the preparation of TMP-loaded HSMC hydrogel. The preferred HSMC in dried state was initially immersed in TMP solution at different concentrations (0.1 mg/mL, 0.5 mg/mL, 1.0 mg/mL, 1.5 mg/mL, and 2.0 mg/mL), and the prepared TMP-loaded HSMC hydrogels were designated as HSMC/TMP-1, HSMC/TMP-2, HSMC/TMP-3, HSMC/TMP-4 and HSMC/TMP-5, respectively.

2.5 Aldehyde content (AC) of OMCC polymer test

Briefly, 0.1 g of freeze-dried OMCC powder was added to the Erlenmeyer flask, and 25 mL of hydroxylamine methanol hydrochloride solution (60 g/L) was added to the above flask, then a small amount of thymol blue methanol solution was added. The reaction solution was heated to 65 °C and stirred for 2 h. After the reaction solution was cooled to room temperature, the sodium hydroxide methanol solution (0.03 mol/L) was used to titrate, the color of the solution changed from pink to yellow. The aldehyde content of OMCC polymer could be calculated as follows;

$$AC = \frac{c_{NaOH-CH3OH}(V_2-V_1)}{2000m/161} \times 100\% \tag{1}$$

Where AC (%) denotes the aldehyde content of OMCC polymer, V_1 denotes the used volume (mL) of sodium hydroxide methanol solution, V_2 denotes the used volume (mL) of sodium hydroxide methanol solution in the control group, $C_{NaOH-CH3OH}$ was 0.03, m denotes the weight of OMCC polymer.

2.6 Fourier infrared spectroscopy (FT-IR) analysis

Fourier transform infrared spectrometer (FT-IR, Nicoet170SX, USA) was used to investigate the functional groups and chemical interactions in HPCS, HPCS-g-SFP, and OMCC polymers as well as HSMC and TMP-loaded HSMC hydrogels. The tested samples were pre-dried using an infrared drying oven, mixed with the potassium bromide powders, grinded, and pressed into thin sections. The FT-IR spectra range was 400-4000 cm^{-1}.

2.7 X-rays Diffraction (XRD) analysis

MCC and OMCC were ground into powder, and X-rays Diffraction (XRD) analysis was conducted using a D8 Advance X-ray diffractometer (Bruker Company, Germany). MCC and OMCC were sprinkled into the sample preparation box of the window as evenly as possible, then the powders were compacted gently with a small spatula to get a very flat plane of the sample powders. Analysis was undertaken at conditions of 40 KV tube pressure, 40 mA tube flow, and 0.02° step length, with scanning performed in the range of 5-45 ° using a copper target nickel filter.

2.8 Degree of substitution SFP of HPCS-*g*-SFP copolymer determination

Ultraviolet spectrophotometry (UV-5500PC, Shanghai Yuanxi Instrument Co., Ltd) was used to determine the degree of substitution (*DS*) of HPCS-*g*-SFP copolymer. First, a series of standard SFP solutions were prepared (0.001, 0.005, 0.01, 0.015, and 0.02 g/L), the absorbances at 190 nm were measured. Based on the correlation coefficient (R^2) of 0.9986, the λ=190 nm was used to investigate the SFP DS of prepared polymer. Then, each HPCS-*g*-SFP sample was subsequently dissolved in deionized water to prepare a solution with a concentration of 0.02 g/L, and the absorbance was measured

at the wavelength of 190 nm [13, 14]. The replacement degree of HPCS-g-SFP copolymer was then calculated as follows;

$$DS = \frac{237A + 17}{13.68A - 62} \quad (2)$$

Where DS (%) denotes the degree of substitution of SFP, A denotes absorbance.

2.9 Free radical scavenging rate test

The clearance rate of HPCS-g-SFP copolymer to free radical (·OH) was tested according to the method described in the literature [37]. Briefly, 1,10-phenanthroline solution (1.5 mmol/L) and ferrous sulfate solution (1.5 mmol/L) were initially prepared. 1.0 mL of the HPCS-g-SFP sample at various concentrations (0.1 g/L, 0.5 g/L, 1.0 g/L, 1.5 g/L, and 2.0 g/L) and 1.0 mL of 1,10-phenanthroline solution were mixed, and then, 1.0 mL of 0.03% hydrogen peroxide solution was added and reacted at 37 °C for 1 h. Since the complex formed by Fe^{2+} and 1,10-phenanthroline has a maximum absorption at the wavelength of 536 nm, the absorbance of the solution at 536 nm after the reaction completion was measured using an ultraviolet spectrophotometer and recorded as A_t. The control group replaced the test sample with 1.0 mL of distilled water, and its absorbance was recorded as A_n. In the blank group, 1.0 mL of distilled water was used to replace hydrogen peroxide, and the absorbance was recorded as A_b. The hydroxyl radical scavenging rate was subsequently calculated as follows;

$$^{\bullet}OH = \frac{A_t - A_n}{A_b - A_n} \times 100\% \quad (3)$$

Where OH denotes the OH clearance rate in percentage. A_t, A_n and A_b (Au) denote the absorbances of HPCS-g-SFP solutions, respectively.

The scavenging rate of HPCS-g-SFP polymer on 1,1-diphenyl-2-picrylhydrazyl radical (DPPH) was also determined in accordance with the method described in the literature[38]. Briefly, DPPH was dissolved in ethanol, and a solution with a concentration of 0.1 mmol/L, was prepared. The test solutions of HPCS-g-SFP polymer in DPPH-ethanol solution with different concentrations (0.1 g/L, 0.5 g/L, 1.0 g/L, 1.5 g/L, and 2.0 g/L) were subsequently prepared. 2.0 mL of each tested solution and 2.0 mL of the DPPH solution where mixed and reacted for 30 min in the dark at 25°C. The absorbance A of the resulting solution was then measured at the wavelength of 517 nm. The control solution was also prepared by mixing 2.0 mL of distilled water and 2.0 mL of DPPH, and its absorbance was subsequently recorded as A_c. The blank group was prepared by mixing 2.0 mL of the HPCS-g-SFP polymer with 2.0 mL of ethanol, and its absorbance was recorded as A_b. The DPPH radical scavenging rate (DPPH) was subsequently calculated as follows;

$$\text{DPPH} = \frac{A_c - A_b}{A_c} \times 100\% \tag{4}$$

Where A_c and A_b (Au) denote the absorbances of the control and blank solutions, respectively.

2.10 Scanning electron microscopy (SEM）

The prepared HSMC-1, HSMC-2, HSMC-3, HSMC-4 and HSMC-5 samples, were initially brittle fracture using liquid nitrogen, then lyophilized. The brittle section of the hydrogel was coated with platinum (Pt) to prevent imaging artifacts from electrical charging. The topography of the section was investigated by Scanning Electron Microscope (SEM, S-4800, Hitachi, Japan).

2.11 Equilibrium swelling rate (ESR) of hydrogels

The mass ($m_{i,1}$ in g) of each freeze-dried HSMC hydrogel was initially determined the inserted in 200mL of distilled water. Each hydrogel sample was then recovered from the distilled water every 20 min, and the surface of the retrieved hydrogel was dried using filter paper and its mass determined. The equilibrium state when the mass of the retrieved hydrogel remains unchanged was noted, and the associated mass of the retrieved and swollen hydrogel ($m_{i,2}$ in g) was determined. The equilibrium swelling rate (ESR) of the sample was then determined as follows;

$$\text{ESR} = \frac{m_{i,2} - m_{i,1}}{m_{i,1}} \times 100\%$$

(5)

Where $m_{i,1}$ and $m_{i,2}$ denote the masses (g) of the ith HSMC hydrogel before immersion in distilled water and at the equilibrium state, respectively.

2.12 Water evaporation rate (WER) of hydrogels

The mass ($m_{i,1}$ in g) of each freeze-dried HSMC hydrogels was initially determined and inserted in distilled water to obtain the mass ($m_{i,2}$ in g) of the swollen HSMC hydrogels at equilibrium state as described in section 2.9 above. The swollen hydrogel was then subjected to air drying at a temperature of 36 °C for 48 h, and the mass ($m_{i,3}$ in g) was determined. The water evaporation rate (WER) of the hydrogel was then calculated as follows;

$$\text{WER} = \frac{m_{i,2} - m_{i,3}}{m_{i,2} - m_{i,1}} \times 100\%$$

(6)

Where $m_{i,1}$, $m_{i,2}$ and $m_{i,3}$ denote the masses (g) of the ith HSMC hydrogel before immersion in distilled water, at the equilibrium state and after evaporation at 36 °C,

respectively.

2.13 Hemocompatibility evaluation

1 mL of fresh blood sample was collected from the rat model using an anticoagulation tube and diluted with 1.25 mL of 0.9 % (mass/volume, 0.9 g of NaCl in 100 mL of Millipore water) normal saline. Then, the HMSC and TMP-loaded HMSC hydrogel were lyophilized and ground into powder. 25 mg of the HMSC tested powder was added to 10 mL of 0.9 % saline (mass/volume) in a test tube, and subsequently incubated in a constant temperature water bath at 37 °C for 30 min. 0.2 mL of diluted blood was then added to the test tube and incubated for 1 h. At the end of the incubation, the mixture was centrifuged at 1000 rpm for 5 min. The absorbance of the supernatant was then measured at the wavelength of 545 nm using an ultraviolet spectrophotometer (UV-5500PC). The positive control group consisted of 10 mL of distilled water mixed with 0.2 mL of diluted blood, and the negative control group consisted of 10 mL of 0.9 % normal saline mixed with 0.2 mL of diluted blood. The hemolysis rate (HR) of the sample was subsequently calculated as follows;

$$HR = \frac{A_t - A_n}{A_p - A_n} \times 100\% \tag{7}$$

Where, A_t is the absorbance of the supernatant of the sample group (Au), A_p is the absorbance of the supernatant of the positive control group (Au), and A_n is the absorbance of the supernatant of the negative control group (Au).

2.14 Cytocompatibility evaluation

Human skin fibroblasts (HSF, PCS-201-012, ATCC) were cultured according to

ATCC instructions, and human hypertrophic scar fibroblasts (HSFB) were supplied by Wuhan No. 1 hospital in China. The cell culture medium for HSFB culture contained a Dulbecco's modified Eagle's medium (DMEM) supplemented with 10 % of fetal bovine serum and 5% of penicillin streptomycin. The cells were cultured in a T25 cell culture flask under a humidified atmosphere of 95% air and 5 % CO_2 at 37 °C. The culture medium was replaced every two days; when cell density reached 80%, cells were digested using trypsin, centrifuged and re-suspended in a new cell medium. The cells produced at the 3rd generation were used for the next *in vitro* experiments. HPCS, HPCS-*g*-SFP polymer, HSMC and TMP-loaded HSMC hydrogels were lyophilized and sterilized with UV for 2 h, then placed in a watch glass with a serum-containing medium at 37 °C for 24 h to re-form the hydrogel. A 0.22 µm filter membrane was then used to filter the extract, with the filtered extract subsequently stored in a fridge at 4 °C for later use. Afterwards, a cell counting kit-8 (CCK-8) was used to evaluate the cytocompatibility of the extract. To assess the cytocompatibility of the extract, 100 µL of the hydrogel extract was added to a 96-well plate, and a 10 µL of cell suspension (*ca.* 1×10^5 cells) was then introduced to each well, after which the plate was transferred to the incubator. After culturing for 1 day, the medium was replaced, and 10 µL of CCK-8 solutions were subsequently added to each well and incubated for 2 h. Finally, the absorbance of the solution was measured at the wavelength of 450 nm with a microplate reader, and the cell survival rate (CV) was calculated as follows;

$$CV = \frac{OD_s - OD_b}{OD_c - OD_b} \times 100\% \tag{8}$$

Where OD_s is the absorbance of experimental wells (containing cells, culture medium, sample extract and the CCK-8 solution); OD_b is the absorbance of blank wells (containing medium and CCK-8 solution, without cells and sample extract); OD_c is the absorbance of the control well (contains cells, culture medium and CCK-8 solution, without the sample extract).

2.15 Animal experiments

The rat models were established according to the method in the literature [37]. 20 *Rattus norvegicus* were randomly numbered after being fed for one week, and the rats were divided into 5 groups (i.e. 4 rats in each group) and designated as A, B, C, D, and E. Group A represented the group treated with normal saline, group B represented the group treated with HPCS solution (5%), group C represented the group treated with HPCS-*g*-SFP polymer solution (5%), group D represented the group injected using HSMC hydrogel, and group E represented the group injected by HSMC/TMP-2 hydrogel. 0.9 mL of 3 % sodium pentobarbital solution was inserted into the abdominal cavity to anaesthetize the rat. The back of the rat was then shaved with an electric shaver. The temperature of the constant temperature electric permeameter was set to 75 °C, and it was applied vertically to the rat's skin, for 15 s, such that a 20-mm wide, deep second-degree burn model was manifested symmetrically on the back of each rat in which the epidermis and the deep layer of the dermis are affected, and photograph of the skin burn model was shown in Figure S1. After then, the wound was treated using different group (A, B, C, D, and E). Pictures were then captured on the days of 7, 14 and 21 d, and the

situation of each wound, with respect to the presence of redness, swelling, scabs, and scars, recorded. To determine the wound healing rate, the wound was covered with a standard transparent grid paper, and the shape of each wound, carefully drawn. The area of the drawn shape was then calculated, and the wound healing rate (WHR) was determined as follows;

$$\text{WHR} = \frac{A_0 - A_{i,t}}{A_0} \times 100\% \tag{9}$$

Where A_0 (m^2) is the wound area on day, 0 (zero), $A_{i,t}$ (m^2) is the wound area on the ith day (i.e. day 7, 14 and 21).

In this study, the wound healing time has been determined by visual observation and the time taken to achieve the recorded healing. Furthermore, the hematoxylin-eosin (HE) staining was investigated on days 0, 7, 14 and 21, and HE images were obtained using an optical microscope.

2.16 Statistical analysis

All experiments were conducted in triplicate, and the data were expressed as means with standard deviation. The SPSS software (SPSS Inc, Chicago IL) was used for the analysis. ANOVA or 2-way repeated-measures ANOVA statistical analyses and Tukey's test were applied to investigate specific differences. Statistical significance was defined at a p-value of < 0.05, < 0.01 and < 0.001 for 95%, 99%, and 99.9 % confidence, respectively.

3. Results and discussion
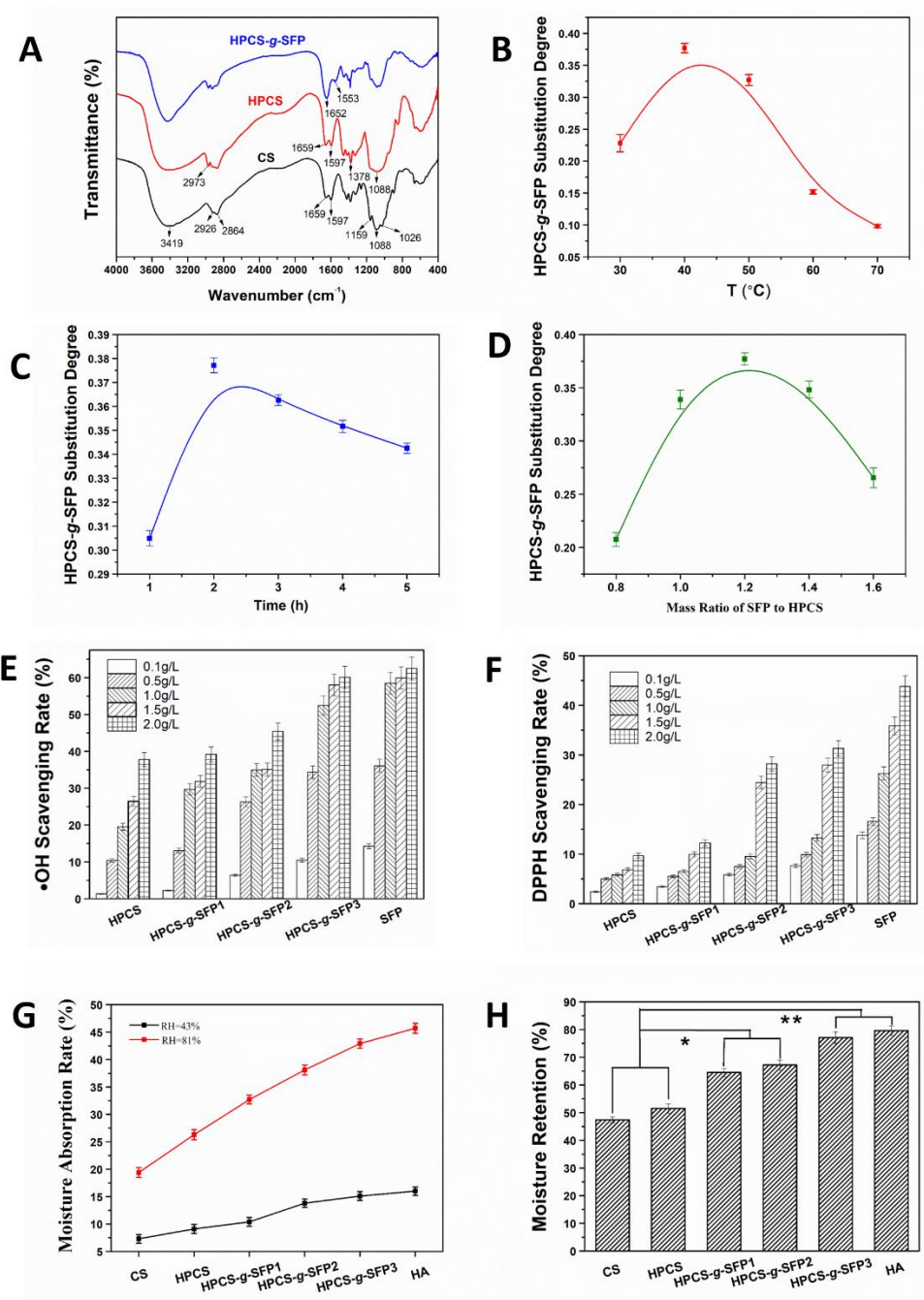
3.1 Polymer characterization results

Figure 1. The characterization of HPCS-*g*-SFP copolymer. A) The FT-IR spectra of chitosan (CS), HPCS, HPCS-*g*-SFP. Substitution degree of SFP on HPCS-*g*-SFP polymer influenced by (B) reaction temperature, (C) time, and (D) mass ration of SFP/HPCS. (E) Hydrogen hydroxyl radicals

and (F) DPPH free radical scavenging ability of HPCS-g-SFP polymers compared to HPCS and SFP polymers. (G) Moisture absorption and (H) moisture retention of HPCS-*g*-SFP polymers in comparison with CS and hyaluronic acid (HA). $^{*}p < 0.05$, $^{**}p < 0.01$.

The results of the characterization of the HPCS-*g*-SFP copolymer is presented in **Figure 1**. **Figure 1A** shows the results of the FT-IR analyses of the HPCS-*g*-SFP, HPCS and CS polymers. It is observed that absorption peaks are present at wavenumbers of 2973 cm^{-1} and 1378 cm^{-1} in the FT-IR spectrum of the HPCS polymer. This observation is due to the stretching vibration and bending vibration absorption peaks of the CH_3 group [39, 40], respectively, and this shows that CH_3 group was successfully introduced to CS [39]. **Figure 1** also showed that the characteristic peaks at 1159 cm^{-1} and 1026 cm^{-1} in the FT-IR spectra of CS, where absent in the FT-IR spectra of HPCS and HPCS-*g*-SFP polymer, while the N-H bending vibration peak at 1597 cm^{-1} did not weaken, indicating that the hydroxypropylation reaction mainly occurs at the C3 and C6 positions of CS[41]. New characteristic peaks were observed at the wavenumbers of 1652 cm^{-1} and 1553 cm^{-1} when the FT-IR spectra of HPCS-*g*-SFP were considered relative to the HPCS spectra. These absorption peaks indicate the presence of amide I and amide II, indicating that the silk fibroin peptide (SFP) was successfully grafted to the hydroxypropyl shell polymer [42]. **Figure 1C-D** also shows that the SFP substitution degree on HPCS-*g*-SFP polymer was influenced by reaction time, temperature and mass ratio of SFP/HPCS. The results show that at 40 °C (**Figure 1 B**), the reaction time was 2 h (**Figure 1 C**), and the feed ratio of SFP/HPCS was 1.2 (**Figure 1 D**), higher degrees of SFP substitutions of the HPCS-*g*-SFP polymer of 0.34, 0.37,

and 0.38, respectively, were observed relative to other conditions investigated. The HPCS-*g*-SFP polymers with SFP substitution degrees of 0.34, 0.37, and 0.38 were designated as HPCS-*g*-SFP1, HPCS-*g*-SFP2, and HPCS-*g*-SFP3 respectively. Given the importance of the hydroxyl radical scavenging rate as an index for evaluating the oxidation resistance, the scavenging ability of the synthesized polymers was investigated (**Figure 1E**). **Figure 1E** shows that a positive correlation exists between an increase in the scavenging ability of HPCS, HPCS-*g*-SFP1, HPCS-*g*-SFP2, HPCS-*g*-SFP3 and SFP and an increase in polymer concentration. SFP was shown to present the highest scavenging ability with a scavenging rate of 62.5% at a solution concentration of 2.0 g/L. HPCS, on the other hand, presented the lowest scavenging ability of 37.8% at a solution concentration of 2.0 g/L. The high scavenging ability of SFP, which translates to favourable antioxidant properties, is because of the presence of various amino acids (such as, glycine, serine) and the unique arrangement of amino acid molecules [43]. This observation is consistent with a previous study that showed that higher SFP contents led to higher hydroxyl radical scavenging rates [44]. Similarly, **Figure 1F** shows the DPPH radical scavenging rate of HPCS, HPCS-*g*-SFP1, HPCS-*g*-SFP2, HPCS-*g*-SFP3, and SFP at different solution concentrations. As expected based on earlier discussions above, **Figure 1F** shows that as polymer concentration increases, the scavenging ability of DPPH free radicals also increases. Similarly, it is also observed that SFP presented the highest DPPH radical scavenging rate of 43.9% at the concentration of 2.0 g/L. In contrast, HPCS has the lowest DPPH radical scavenging rate of 9.6% at a concentration of 2.0 g/L.

Further consideration of **Figure 1** shows that the polymers exhibited varying moisture absorption rates. **Figure 1G** shows that when a relative humidity of 43% is imposed, the moisture absorption rates of CS, HPCS, HPCS-*g*-SFP1, HPCS-*g*-SFP2, HPCS-*g*-SFP3, and HA were 7.3%, 9.1%, 10.4%, 13.8%, 15.1% and 16.0%, respectively. This observation suggests that the moisture absorption rate increases with increasing the SFP substitution degree, which translates to an increased number of "available" functional hydroxyl groups for secondary bond formation via hydrogen bonds. As expected, the imposition of a higher relative humidity of 81 % translated to higher moisture absorption rates for the polymers of CS, HPCS, HPCS-*g*-SFP1, HPCS-*g*-SFP2, HPCS-*g*-SFP3, and HA of 19.4%, 26.3%, 32.7%, 38.1%, 42.9%, and 45.7%, respectively. This observation is because higher relative humidity translates to higher moisture availability in the environment for absorption by the polymers. Similarly, the moisture retention abilities of CS, HPCS, HPCS-*g*-SFP, and HA were also analysed, and the results presented in **Figure 1H**. Similar trends to the moisture adsorption rate (**Figure 1G**) were observed when moisture retention was considered. This observation is due to the presence of hydrophilic functional groups (i.e. OH) that facilitate secondary bond formation with water molecules. The results presented in **Figure 1G** and **Figure 1H** highlight the significant moisture absorption and moisture retention properties of the HPCS-g-SFP copolymer, indicating the polymer facilitates moisture retention during the wound healing process and thus has potential for use in wound dressing [45].

3.2 Characterization of oxidized microcrystalline cellulose (OMCC)

OMCC was synthesized via a strong oxidation reaction of microcrystalline cellulose (MCC) shown in **Scheme 1B**. The aldehyde content of prepared OMCC was around 73%, and MCC and OMCC were further investigated using XRD and FT-IR, the results were presented in **Figure 2.**
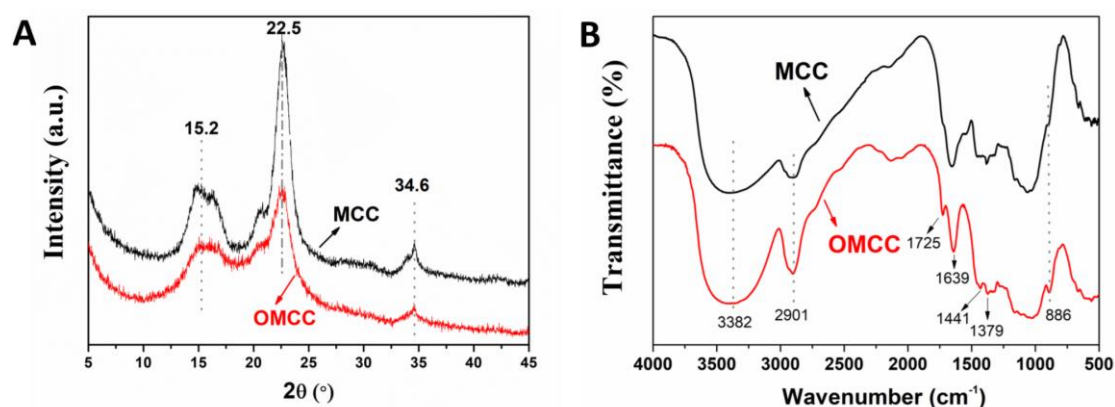

Figure 2. (A) XRD spectrum and (B) FT-IR spectrum of MCC and OMCC.

Figure 2A shows the XRD patterns of MCC and OMCC. It is observed that the shapes and diffraction angles for the XRD spectrum of MCC and OMCC are similar. Crystalline and amorphous regions in the molecular structure of MCC with three sharp diffraction peaks in the crystalline region observed [46]. After the oxidation of MCC, the diffraction angle of OMCC remained essentially unchanged, indicating that the oxidation reaction did not change its crystalline structure [47]. A consideration of the FT-IR spectra of the MCC and OMCC presented in **Figure 2B**, shows that a new peak at 1725 cm^{-1} is observed in OMCC after the oxidation of MCC. This observation shows that the hydroxyl group on the MCC had undergone an oxidation reaction to form an aldehyde group [36].
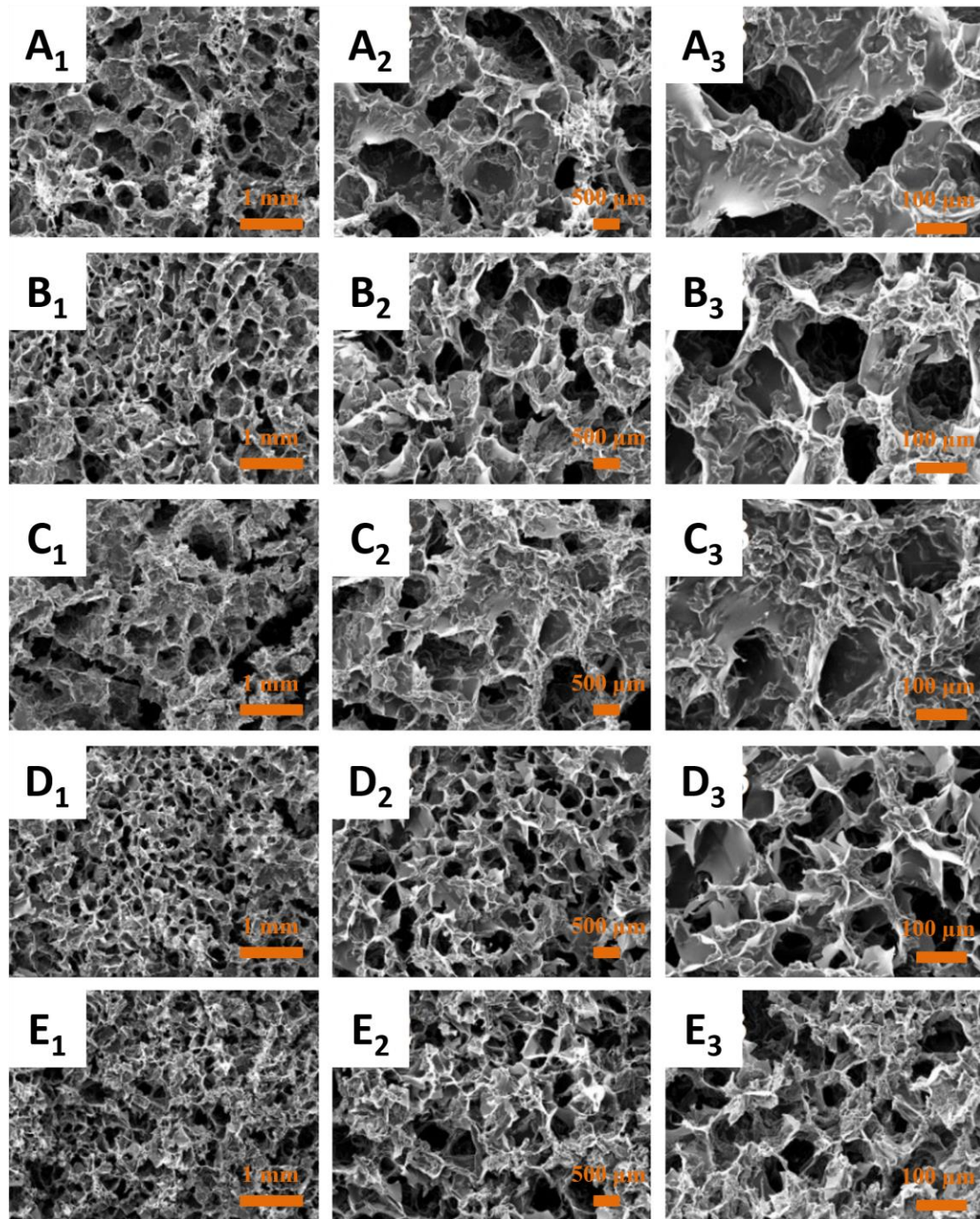
Figure 3. SEM images of freeze-dried HSMC hydrogels at different magnifications. HSMC-1 (A_1-A_3), HSMC-2 (B_1-B_3), HSMC-3 (C_1-C_3), HSMC-4 (D_1-D_3), and HSMC-5 (E_1-E_3).

3.3 Porous structure of HSMC hydrogels

Figure 3 shows the SEM images of the freeze-dried HSMC hydrogels. The pore distributions of hydrogels were calculated via five SEM images for each sample using

Image J software. The porous structure was shown for all HSMC hydrogels, and such structure facilitates the delivery of drug during the wound healing process. With the crease of OMCC mass introduced in HSMC hydrogels, the pore size of HSMC hydrogels was decreased. As the mass of OMCC in HSMC hydrogels increased, more available aldehyde groups for reacting with the amino groups on the HPCS-*g*-SFP molecular chain, thus increased the cross-linking degree of hydrogel. The resultant three-dimensional (3D) network structure of the HSMC hydrogel presented the structural basis for its application in wound dressings. The 3D structure could make the hydrogel have a specific water absorption rate, absorb wound exudate and keep the wound surface in a relatively moist environment, which facilitates the migration of cells to promote wound healing [48].
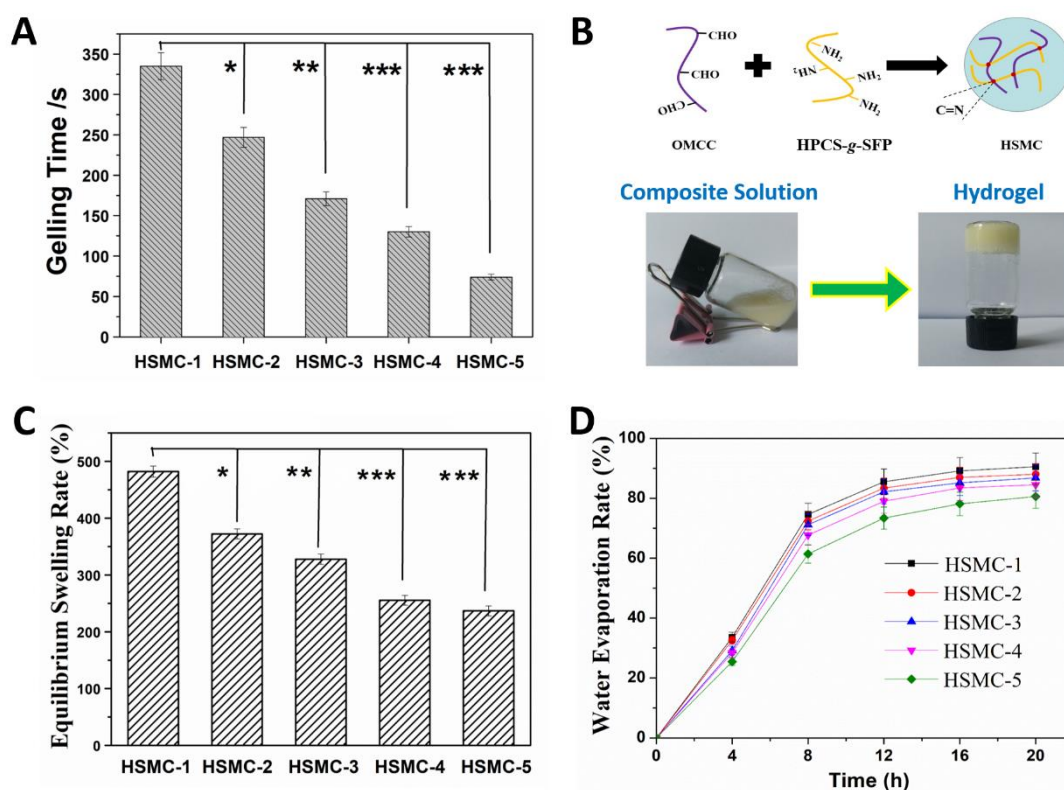

Figure 4. (A) Sol-gel transition times (gelling times) of HSMC hydrogels. (B) Schematic diagram

of the sol-gel transition process. (C) Equilibrium swelling rate and (D) water evaporation rate of HSMC hydrogels. $^{*}p < 0.05$, $^{**}p < 0.01$, and $^{***}p < 0.001$.

3.4 Injectable hydrogel characterization

Recognizing the importance of sol-gel transition time (gelling time) as an important performance indicator of injectable hydrogels, the gelling times of the injectable HSMC hydrogels were assessed using the tube inversion method [49, 50] and the results presented in **Figure 4A**. The gelling time of the prepared HSMC hydrogels ranged from 74 s to 35 s. Notably, as the ratio of OMCC to HPCS-*g*-SFP increases, the content of aldehyde groups in the hydrogel increases. Basic chemical kinetics highlights that the higher content of aldehyde groups will increase the rate of reaction between aldehyde groups and amino groups, leading to shorter gelling time (**Figure 4B**). The HSMC solution could be injected using injector, the hydrogel was formed due to the Schiff base bonds during the sol-gel transition, and such injectable hydrogels favour the utility of hydrogels in wound healing applications.

The equilibrium swelling of the HSMC hydrogels was also evaluated, as shown in **Figure 4C**, the results showed that the equilibrium swelling rates of HSMC-1, HSMC-2, HSMC-3, HSMC-4 and HSMC-5 were 482%, 372%, 328%, 255% and 237%, respectively, indicating that all HSMC hydrogels had good water absorption properties. The increase in the content of OMCC in HSMC hydrogels presented negative effects on the equilibrium swelling rate of hydrogel. This observation is because as the content of OMCC increases, the internal structure of the hydrogel becomes denser, thus

negatively impacting its water absorption ability. Furthermore, the water evaporation rate of the HSMC hydrogel was investigated with the results shown in **Figure 4D**. It is observed that the water evaporation rate of the HSMC hydrogel increases rapidly in the first 8 h, then gradually reduces until the equilibrium state is attained (at 20 h). As the content of OMCC increases from 1.0/1.0 to 3.0/1.0, the water retention performance increases from 238% to 485%. This observation is due to the increase in the cross-linking degree of the hydrogel with increasing OMCC content, leading to a denser internal structure that would inhibit mass transfer, thus preventing the evaporation of water.
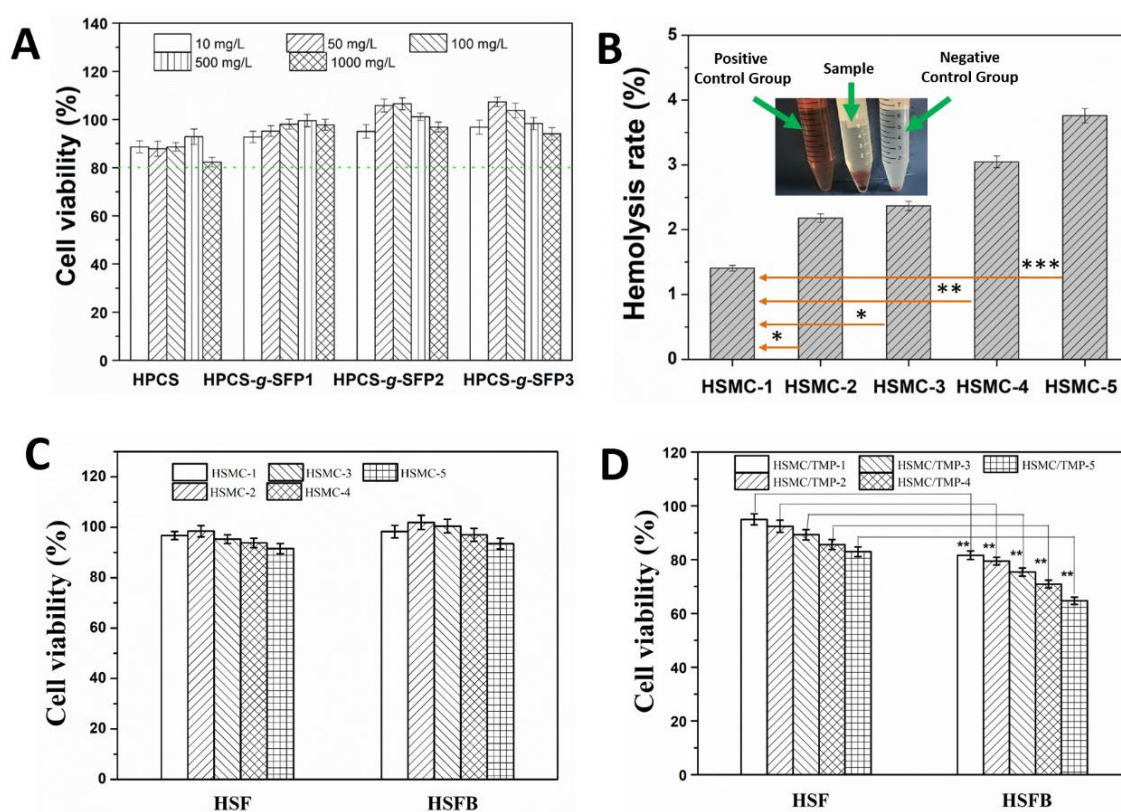

Figure 5. (A) Cytocompatibility of HPCS-*g*-SFP copolymer evaluated by CCK-8 assay after culturing with human skin fibroblasts (HSF) for 24 h. (B) Hemolysis rate analysis of HSMC hydrogels using rat flesh blood. Cytocompatibility of (C) HSMC hydrogels and (D) TMP-loaded

HSMC hydrogels was investigated by CCK-8 assay after culturing with HSF and human hyperplastic scar fibroblasts (HSFB) for 24h. $^*p < 0.05$, $^{**}p < 0.01$, and $^{***}p < 0.001$.

3.5 In vitro tests

The prepared hydrogels were used as wound dressing for wound healing, the extracts of hydrogels were used for culturing with human skin fibroblasts (HSF) and human hyperplastic scar fibroblasts (HSFB) to evaluate their cyctocompatibility [51, 52]. Cell counting kit-8 (CCK-8) was used to investigate the cytocompatibility of HPCS-*g*-SFP copolymer, HSMC and TMP-loaded HSMC hydrogels by culturing the hydrogels extracts with HSF and HSFB, and the results were presented in **Figure 5A**. The cell survival rate of HSF was above 80% after culturing with HPCS-*g*-SFP copolymers at different concentrations. The observation indicates that the hydrogel is not toxic to cells since its survival rate exceeds 80% [53]. In addition, the cell survival rate was higher while culturing was undertaken with HPCS-*g*-SFP copolymer compared to culturing with HPCS polymer, which mainly due to that the amino acid structure of SFP promoted cell adhesion and proliferation. Interestingly, as the concentration of the HPCS-*g*-SFP copolymer extract increased, the cell survival rate initially increased and then decreased. The decrease of cell survival rate may be related to the change of cell osmotic pressure caused by increased HPCS-*g*-SFP copolymer concentration. Furthermore, the excellent cytocompatibility of HPCS-*g*-SFP, HSMC and TMP-loaded HSMC hydrogels was also confirmed by culturing the hydrogels with human bone marrow-derived mesenchymal stem cells (hBMSCs) (**Figure S2**). Over days, the hBMSCs could proliferated on HPCS-g-SFP, HSMC and TMP-loaded HSMC

hydrogels, indicating that the prepared hydrogels could be used in wide biomedical applications.

Additionally, the hemolysis rate of HSMC hydrogels was investigated with the results presented in **Figure 5B**. The result shows that the hemolysis rate of HSMC hydrogel increases as the content OMCC in the HSMC hydrogel increases, with the maximum hemolysis rate, determined to be 3.76%. Crucially, the obtained hemolysis rate values were less than 5%, which was considered the threshold stipulated by the Food and Drug Administration (FDA), indicating the HSMC hydrogel has good cell compatibility [54]. The cytocompatibility of HSMC hydrogel was further evaluated by culturing with HSF or HSFB for 24 h, as shown in **Figure 5C**. After culturing with HSMC hydrogel extracts for 24 h, both survival rates of HSF and HSFB were greater than 90%, indicating all HSMC samples had excellent cytocompatibility. The CCK-8 analysis of TMP-loaded HSMC hydrogels (**Figure 5D**) showed that the survival rate of HSF cells remained above 80% after culturing with all HSMC/TMP composite hydrogel extracts, confirming that the TMP-loaded HSMC hydrogels were not toxic on HSF cells. However, the survival rate of HSFB cells after culturing with TMP-loaded HSMC hydrogel extracts was lower than that of HSF cells, mainly in the range of 64.7-81.63 %, suggesting that TMP-loaded HSMC hydrogel could inhibit the growth of scar fibroblasts.
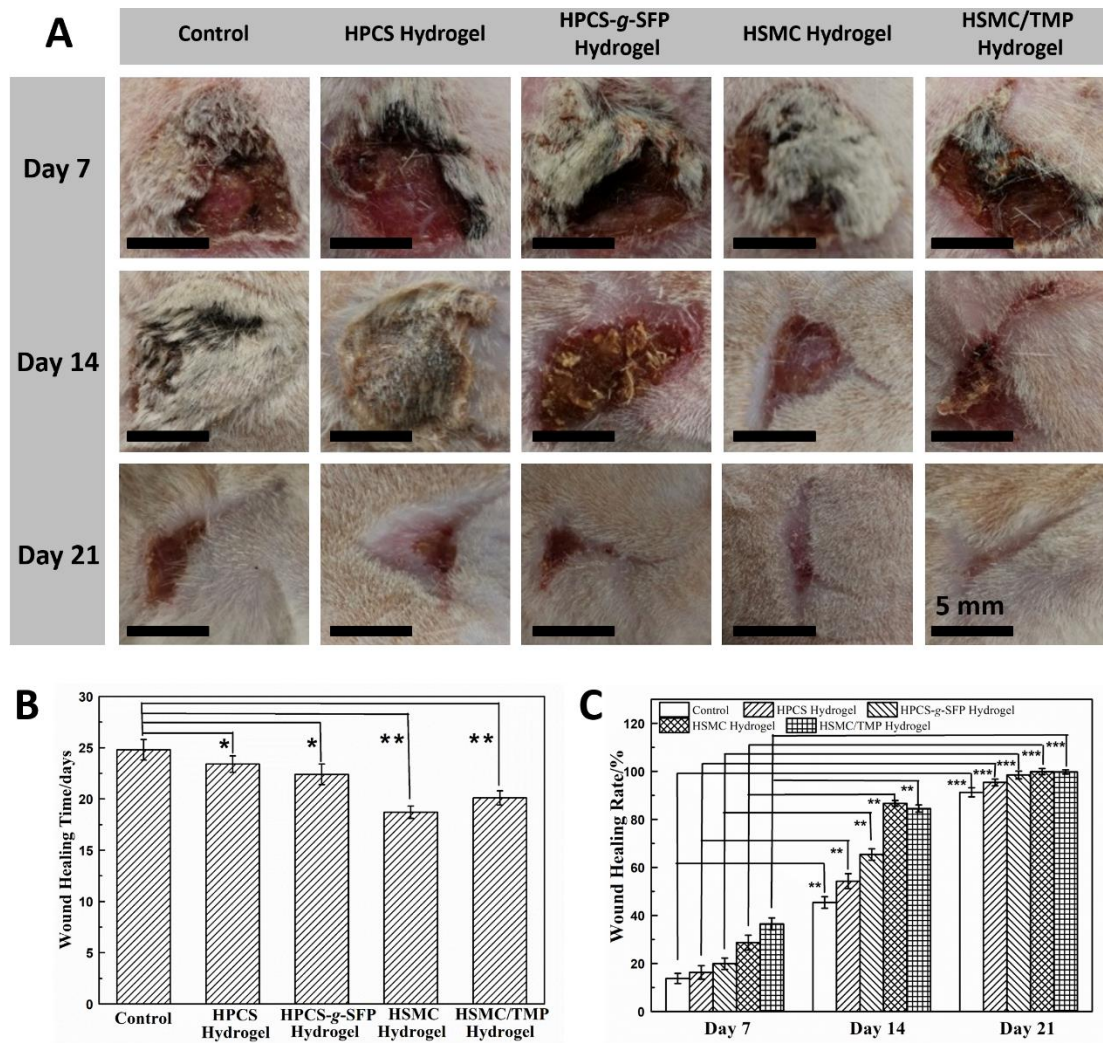
Figure 6. (A) Photographs of the regenerated skin wounds on days 7, 14, and 21 for different groups. (B) The statistical wound healing time and (C) wound healing rate of rats for different groups, the wounded skin without treatment as the control group. $^{*}p < 0.05$, $^{**}p < 0.01$, and $^{***}p < 0.001$.

3.6 In vivo wound healing

A deep second-degree burn was introduced on the back of the rat model to evaluate the efficacy of the prepared hydrogels as wound dressings, the appearance of wounds in each group on days 7, 14, and 21 are presented in **Figure 6A.** After the skin burn model was formed, the forming time was considered as day 0, the photo of skin burn model was shown in **Figure S1**. On day 7, the wounds of all groups shrunk, with the

edges of the wounds visible, and all scabs were formed. Redness of the wound was, however, still observed. The displayed appearance was mainly due to skin spasm caused by deep burns and the deformation effect of pressure on the skin during film formation [55]. The color of wounds for HSMC and TMP-loaded HSMC hydrogels was darker than that of the normal saline group. On day 14, the wounds of each group were relatively dry with no obvious exudation. The wounds for the saline and HPCS groups had smaller shrinkage than other groups, and the surface scabs still existed. The formation of new granulation tissue was observed in the wounds for the HPCS-*g*-SFP group, HSMC hydrogel group and TMP-loaded HSMC hydrogel group, but the new granulation tissue was not completely epithelialized. On day 21, the wounds for all groups had shrunk significantly. The wounds for HSMC hydrogel and TMP-loaded HSMC hydrogel groups were completely healed. The observed scar in the TMP-loaded HSMC hydrogel group was considerably smaller than that of other groups, and the small wounds could be observed in the saline group, HPCS group and HPCS-*g*-SFP group. **Figure 6A**, therefore, shows that HPCS-*g*-SFP, HSMC, and TMP-loaded HSMC hydrogel present favourable effects on burn wound healing, and the addition of TMP could effectively reduce the formation of scar tissue.

In addition, the wound healing time (**Figure 6B**) and wound healing rate (**Figure 6C**) for the five test groups were also investigated. The healing time for the normal saline group, HPCS hydrogel group, HPCS-*g*-SFP hydrogel group, HSMC hydrogel group, TMP-loaded HSMC hydrogel group were 25, 23, 22, 18, and 20 days, respectively. The HSMC hydrogel group displayed the shortest healing time of 18 days.

The healing time of the TMP-loaded HSMC hydrogel group was slightly longer than that of the HSMC group, since TMP could inhibit the excessive proliferation of fibroblasts; thus, prolonging the time required to recover the wound skin. **Figure 6C** shows the wound healing rate of each test group on the 7, 14 and 21 days. On day 7, the wound healing rate of each group was low, and the healing rate of the TMP-loaded HSMC hydrogel group reached the maximum value of 36.5%. On day 14, the healing rate of each group increased significantly, and the healing rate of each group ranged from 45.2% to 86.7%. On day 21, the wound healing rates for all groups were greater than 90%, and the wound healing rate of the HSMC and TMP-loaded HSMC hydrogel groups was both ~100%, indicating that complete healing was achieved. It is also observed that the healing rate of the HSMC hydrogel on day 7 was lower than that of the TMP-loaded HSMC hydrogel group. However, on day 14, the healing rate of HSMC hydrogel was higher than that of the TMP-loaded HSMC hydrogel group. This observation indicated that TMP might inhibit the excessive proliferation of fibroblasts and display anti-inflammatory effects. The wound treated by TMP-loaded HSMC hydrogel may quickly eliminate the inflammatory cells, enabling the wound area to transition to the fibroblast's proliferation phase rapidly. However, TMP-loaded HSMC hydrogel inhibits excessive proliferation; thus, the proliferation rate of wound fibroblasts in the TMP-loaded HSMC hydrogel group was lower than that in the HSMC hydrogel group.
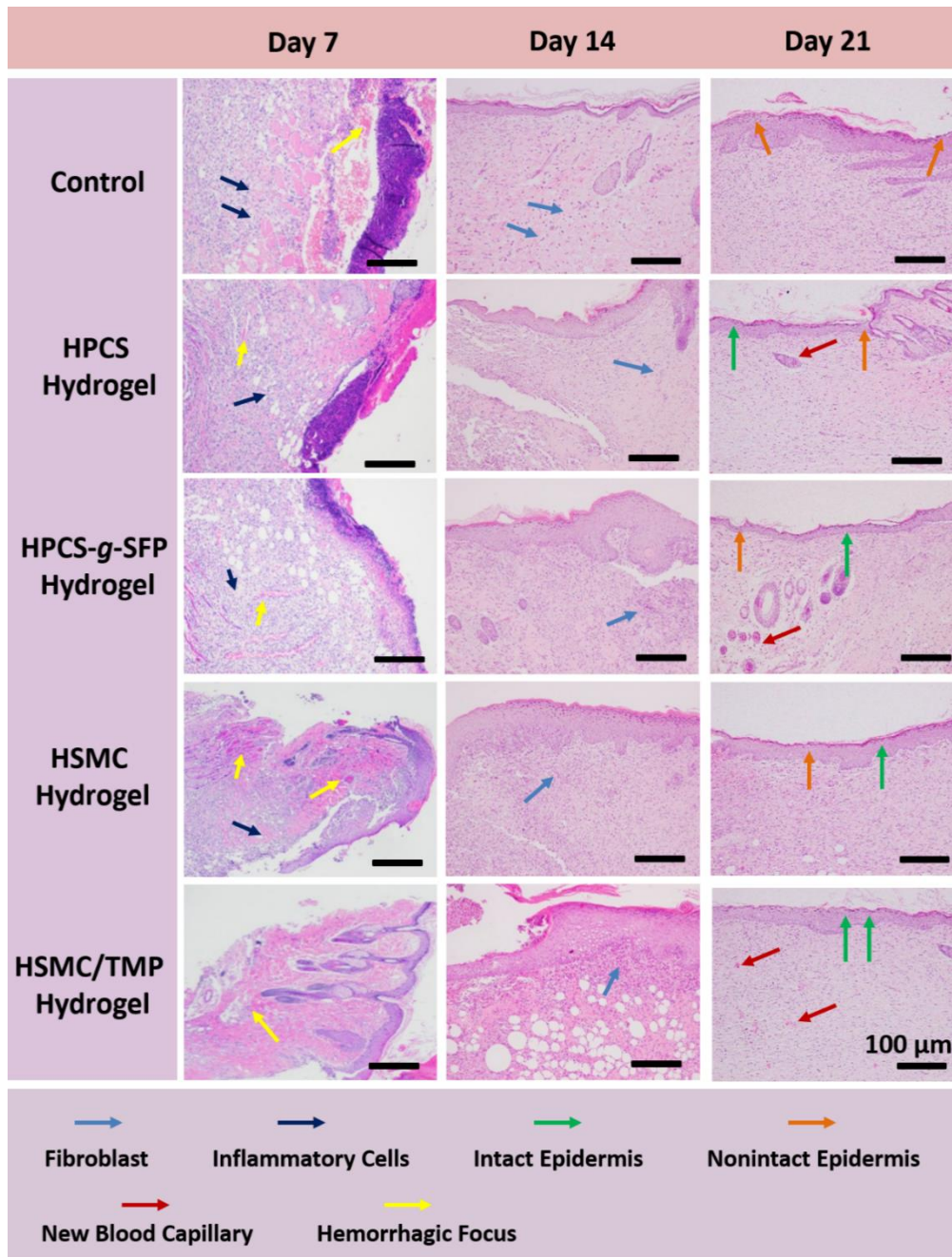
Figure 7. Representative microscope images of HE staining of the newly regenerated skin tissues for each group on days 7, 14, and 21, and the control group with saline treatment.

3.7 Histological analysis

Further analysis of the biological activity was achieved via HE staining tests, including inflammation, angiogenesis, and wound formation, and the results presented

in **Figure 7**. On day 7, the HE staining images of the skin tissues of the wounds in each group had obvious scabs with varying degrees of inflammatory cell infiltration. A large number of lymphocytes and macrophages were migrated into the wound area, and the color of HE staining images at wound areas on day 7 was deep, causing an acute inflammatory response occurred [56]. Notably, more inflammatory cells were observed in the saline and HPCS groups than the HPCS-g-SFP hydrogel, HSMC hydrogel, and TMP-loaded HSMC hydrogel groups, indicating that the saline and HPCS groups had more severe wound inflammation. The fewer inflammatory cells in the HSMC hydrogel and TMP-loaded HSMC hydrogel groups also highlighted the growth of fibroblasts. On day 14, although the crust for the saline group and the HPCS group had not completely fallen off, the scab was not observed. Fibroblasts, epidermal cells and capillaries are present in the HE staining images on all groups. Crucially, few inflammatory cells were observed in the saline group and HPCS group, and the number of fibroblasts and epidermal cells was relatively less. Granulation tissue formation was also observed on the wounds of the HPCS-*g*-SFP group but was not completely epithelialized. A large number of fibroblasts, capillaries and collagen fibers were observed in the HSMC hydrogel and TMP-loaded HSMC hydrogel groups. On day 21, the epidermis of the wounds on the rat models in each group was formed, a large number of fibroblasts proliferated, and collagen fibers also formed. In the saline and HPCS groups, the epidermis was irregular, and the content of collagen fibers was relatively small. A uniform epidermal layer and many capillaries and collagen fibers were formed in HPCS-*g*-SFP. It was observed that the wounds in the HSMC hydrogel and TMP-loaded

HSMC hydrogel groups have complete skin tissue. Compared to the HSMC hydrogel group, the TMP-loaded HSMC hydrogel group had fewer collagen fibers and was arranged parallel to the wound surface. This result reinforced the viability of employing the TMP-loaded HSMC hydrogel to facilitate scarless wound healing. The formation of scars is generally due to the excessive proliferation of fibroblasts induced by wound inflammation, leading to hypertrophic scars at the wound site [57]. TMP has anti-inflammatory and inhibits the excessive proliferation of fibroblasts, so it has the ability to inhibit scarring [58]. The obtained results confirmed that TMP-loaded HSMC hydrogels could promote wound healing without scar formation.

4. Conclusion

In summary, this paper successfully produced an injectable hydrogel capable of facilitating scarless wound healing. The HMSC hydrogel was prepared based on the Schiff base reaction of HPCS-*g*-SFP copolymer and OMCC. The obtained HMSC hydrogels exhibited good swelling and water retention properties and excellent biocompatibility. The TMP-loaded HSMC hydrogel was shown to have good biological activity. The CCK-8 test of HSF and HFSB cells showed that the TMP-loaded HSMC hydrogel facilitated up to 95% cell activity retention. In addition, the animal experiments showed that although HMSC hydrogel had faster healing efficiency than TMP-loaded HSMC hydrogel, TMP-loaded HSMC hydrogel facilitated wound healing in the absence of scars. Thus, TMP-loaded HMSC hydrogel was established as having the potential to promote wound healing while also preventing wound scars.

Declaration of competing interest

I would like to declare on behalf of my co-authors that we have no known competing financial interests or personal relationships that could have appeared to influence the work reported in this paper.

Acknowledgements

References

[1] A.C. Gonzalez, T.F. Costa, Z.A. Andrade, A.R. Medrado, Wound healing - A literature review, An Bras Dermatol, 91 (2016) 614-620.

[2] A. Shavandi, S. Hosseini, O.V. Okoro, L. Nie, F.E. Babadi, F. Melchels, 3D Bioprinting of Lignocellulosic Biomaterials, Advanced Healthcare Materials, 9 (2020).

[3] L. Nie, Q.Y. Wu, H.Y. Long, K.H. Hu, P. Li, C. Wang, M. Sun, J. Dong, X.Y. Wei, J.P. Suo, D.L. Hua, S.L. Liu, H.Y. Yuan, S.F. Yang, Development of chitosan/gelatin hydrogels incorporation of biphasic calcium phosphate nanoparticles for bone tissue engineering, J Biomat Sci-Polym E, 30 (2019) 1636-1657.

[4] L. Nie, Y.L. Deng, P. Li, R.X. Hou, A. Shavandi, S.F. Yang, Hydroxyethyl Chitosan-Reinforced Polyvinyl Alcohol/Biphasic Calcium Phosphate Hydrogels for Bone Regeneration, Acs Omega, 5 (2020) 10948-10957.

[5] D. Chen, C. Zhang, H. Huo, C. Ji, M. Sun, L. Nie, Injectable temperature-sensitive hydrogel with VEGF loaded microspheres for vascularization and bone regeneration of femoral head necrosis, Mater Lett, 229 (2018) 138-141.

[6] P. Safarzadeh Kozani, P. Safarzadeh Kozani, M. Hamidi, O. Valentine Okoro, M. Eskandani, M. Jaymand, Polysaccharide-based hydrogels: properties, advantages, challenges, and optimization methods for applications in regenerative medicine, International Journal of Polymeric Materials and Polymeric Biomaterials, (2021) 1-15.

[7] M. Chen, J. Tian, Y. Liu, H. Cao, R. Li, J. Wang, J. Wu, Q. Zhang, Dynamic covalent constructed self-healing hydrogel for sequential delivery of antibacterial agent and growth factor in wound healing, Chemical Engineering Journal, 373 (2019) 413-424.

[8] F. Kong, C. Fan, Y. Yang, B.H. Lee, K. Wei, 5-hydroxymethylfurfural-embedded poly (vinyl alcohol)/sodium alginate hybrid hydrogels accelerate wound healing, International Journal of Biological Macromolecules, 138 (2019) 933-949.

[9] T. Wang, F. Zhang, R. Zhao, C. Wang, K. Hu, Y. Sun, C. Politis, A. Shavandi, L. Nie, Polyvinyl Alcohol/Sodium Alginate Hydrogels Incorporated with Silver Nanoclusters via Green Tea Extract for Antibacterial Applications, Designed Monomers and Polymers, 23 (2020) 118-133.

[10] M. Hamidi, O.V. Okoro, P.B. Milan, M.R. Khalili, H. Samadian, L. Nie, A.J.C.P. Shavandi, Fungal exopolysaccharides: Properties, sources, modifications, and biomedical applications, (2022) 119152.

[11] O.V. Okoro, A. Amenaghawon, D. Podstawczyk, H. Alimoradi, M.R. Khalili, M. Anwar, P.B. Milan, L. Nie, A. Shavandi, Fruit pomace-lignin as a sustainable biopolymer for biomedical applications, Journal of Cleaner Production, 328 (2021) 129498.

[12] H. Li, W. Cheng, K. Liu, L. Chen, Y. Huang, X. Wang, Z. Lv, J. He, C. Li, Reinforced collagen with oxidized microcrystalline cellulose shows improved hemostatic effects, Carbohydrate Polymers, 165 (2017) 30-38.

[13] W. Hu, M. Liu, X. Yang, C. Zhang, H. Zhou, W. Xie, L. Fan, M. Nie, Modification of chitosan grafted with collagen peptide by enzyme crosslinking, Carbohydrate Polymers, 206 (2019) 468-475.

[14] L. Min, M. Liu, L. Liu, Z. Rao, C. Zhu, L. Fan, Enzymatic synthesis of quaternary ammonium chitosan-silk fibroin peptide copolymer and its characterization, International Journal of Biological Macromolecules, 109 (2018) 1125-1131.

[15] M.-C. Miller, J. Nanchahal, Advances in the Modulation of Cutaneous Wound Healing and Scarring, BioDrugs, 19 (2005) 363-381.

[16] R. Ogawa, Keloid and Hypertrophic Scars Are the Result of Chronic Inflammation in the Reticular Dermis, Int J Mol Sci, 18 (2017).

[17] J. Canady, S. Karrer, M. Fleck, A.K. Bosserhoff, Fibrosing connective tissue disorders of the skin: molecular similarities and distinctions, J Dermatol Sci, 70 (2013) 151-158.

[18] F. Reno, M. Sabbatini, F. Lombardi, M. Stella, C. Pezzuto, G. Magliacani, M. Cannas, In vitro mechanical compression induces apoptosis and regulates cytokines release in hypertrophic scars, Wound Repair Regen, 11 (2003) 331-336.

[19] H.J. Lee, Y.J. Jang, Recent Understandings of Biology, Prophylaxis and Treatment Strategies for Hypertrophic Scars and Keloids, Int J Mol Sci, 19 (2018).

[20] G.R. Melles, P.S. Binder, W.H. Beekhuis, R.H. Wijdh, M.N. Moore, J.A. Anderson, N. SundarRaj, Scar tissue orientation in unsutured and sutured corneal wound healing, Br J Ophthalmol, 79 (1995) 760-765.

[21] S.J. Maleki, J.F. Crespo, B. Cabanillas, Anti-inflammatory effects of flavonoids, Food Chem, 299 (2019) 125124.

[22] H.M. Powell, B. Nedelec, Mechanomodulation of Burn Scarring Via Pressure Therapy, Adv Wound Care (New Rochelle), 11 (2022) 179-191.

[23] J.S. Bond, J.A.L. Duncan, T. Mason, A. Sattar, A. Boanas, S. O'Kane, M.W.J. Ferguson, Scar Redness in Humans: How Long Does It Persist after Incisional and Excisional Wounding?, Plastic and Reconstructive Surgery, 121 (2008).

[24] T.T. Phan, I.J. Lim, L. Sun, S.Y. Chan, B.H. Bay, E.K. Tan, S.T. Lee, Quercetin inhibits fibronectin production by keloid-derived fibroblasts. Implication for the treatment of excessive scars, J Dermatol Sci, 33 (2003) 192-194.

[25] J.W. Cho, S.Y. Cho, S.R. Lee, K.S. Lee, Onion extract and quercetin induce matrix metalloproteinase-1 in vitro and in vivo, Int J Mol Med, 25 (2010) 347-352.

[26] A.S. Abouheba Mohamed, E. Edward Michael, R. Carachi, KERATINOCYTE REGULATION OF FIBROBLAST TRANSFORMING GROWTH FACTOR BETA EXPRESSION: CAN OUR WOUNDS HEAL WITHOUT A SCAR?, Journal of Urology, 181 (2009) 256-256.

[27] M. Sisco, Z.B. Kryger, K.D. O'Shaughnessy, P.S. Kim, G.S. Schultz, X.-Z. Ding, N.K. Roy, N.M. Dean, T.A. Mustoe, Antisense inhibition of connective tissue growth factor (CTGF/CCN2) mRNA limits hypertrophic scarring without affecting wound healing in vivo, Wound Repair and Regeneration, 16 (2008) 661-673.

[28] L. Dai, R. Diao, J. Zhang, M. Cao, H. Gao, B. Tang, Tetramethyl pyrazine exerts anti-apoptotic and antioxidant effects in a mouse model of MPTP-induced Parkinson's disease via regulation of the expressions of Bax, Bcl-2, Nrf2 and GCLC, Tropical Journal of Pharmaceutical Research, 20 (2021).

[29] M. Zhong, W. Ma, X. Zhang, Y. Wang, X. Gao, Tetramethyl pyrazine protects hippocampal neurons against anoxia/reoxygenation injury through inhibiting apoptosis mediated by JNK/MARK signal pathway, Medical Science Monitor: International Medical Journal of Experimental and Clinical Research, 22 (2016) 5082.

[30] F. Zhang, C. Ni, D. Kong, X. Zhang, X. Zhu, L. Chen, Y. Lu, S. Zheng, Ligustrazine attenuates oxidative stress-induced activation of hepatic stellate cells by interrupting platelet-derived growth factor-β receptor-mediated ERK and p38 pathways, Toxicology and applied pharmacology, 265 (2012) 51-60.

[31] J. Duan, D. Xiang, H. Luo, G. Wang, Y. Ye, C. Yu, X. Li, Tetramethylpyrazine suppresses lipid accumulation in macrophages via upregulation of the ATP-binding cassette transporters and downregulation of scavenger receptors, Oncology reports, 38 (2017) 2267-2276.

[32] W.F. Bi, H.Y. Yang, J.C. Liu, T.H. Cheng, C.H. Chen, C.M. Shih, H. Lin, T.C. Wang, W.S. Lian, J.J. Chen, H.C. Chiu, N.C. Chang, Inhibition of cyclic strain-induced endothelin-1 secretion by tetramethylpyrazine, Clin Exp Pharmacol Physiol, 32 (2005) 536-540.

[33] M. Guo, Y. Liu, D. Shi, Cardiovascular actions and therapeutic potential of tetramethylpyrazine (active component isolated from Rhizoma Chuanxiong): roles and mechanisms, BioMed Research International, 2016 (2016).

[34] W. Hu, M. Liu, X. Yang, C. Zhang, H. Zhou, W. Xie, L. Fan, M. Nie, Modification of chitosan grafted with collagen peptide by enzyme crosslinking, Carbohydr Polym, 206 (2019) 468-475.

[35] K. Kosciow, U. Deppenmeier, Characterization of three novel β-galactosidases from Akkermansia muciniphila involved in mucin degradation, International Journal of Biological Macromolecules, 149 (2020) 331-340.

[36] J. Hao, S. Xu, N. Xu, D. Li, R.J. Linhardt, Z. Zhang, Impact of degree of oxidation on the

physicochemical properties of microcrystalline cellulose, Carbohydr Polym, 155 (2017) 483-490.

[37] Z. Li, B. Wang, Q. Zhang, Y. Qu, H. Xu, G. Li, Preparation and antioxidant property of extract and semipurified fractions of Caulerpa racemosa, Journal of applied phycology, 24 (2012) 1527-1536.

[38] S. Zhang, J. Hou, Q. Yuan, P. Xin, H. Cheng, Z. Gu, J. Wu, Arginine derivatives assist dopamine-hyaluronic acid hybrid hydrogels to have enhanced antioxidant activity for wound healing, Chemical Engineering Journal, 392 (2020) 123775.

[39] M. Prabaharan, J.F. Mano, Hydroxypropyl chitosan bearing beta-cyclodextrin cavities: synthesis and slow release of its inclusion complex with a model hydrophobic drug, Macromol Biosci, 5 (2005) 965-973.

[40] O.V. Okoro, Z. Sun, The characterisation of biochar and biocrude products of the hydrothermal liquefaction of raw digestate biomass, Biomass Conversion and Biorefinery, 11 (2021) 2947-2961.

[41] L.A. Pereira, L. da Silva Reis, F.A. Batista, A.N. Mendes, J.A. Osajima, E.C. Silva-Filho, Biological properties of chitosan derivatives associated with the ceftazidime drug, Carbohydrate polymers, 222 (2019) 115002.

[42] C. Zhu, S. Zou, Z. Rao, L. Min, M. Liu, L. Liu, L. Fan, Preparation and characterization of hydroxypropyl chitosan modified with nisin, Int J Biol Macromol, 105 (2017) 1017-1024.

[43] S.W. Ha, H.S. Gracz, A.E. Tonelli, S.M. Hudson, Structural study of irregular amino acid sequences in the heavy chain of Bombyx mori silk fibroin, Biomacromolecules, 6 (2005) 2563-2569.

[44] M. Liu, L. Min, C. Zhu, Z. Rao, L. Liu, W. Xu, P. Luo, L. Fan, Preparation, characterization and antioxidant activity of silk peptides grafted carboxymethyl chitosan, Int J Biol Macromol, 104 (2017) 732-738.

[45] H.C. Korting, C. Schollmann, R.J. White, Management of minor acute cutaneous wounds: importance of wound healing in a moist environment, J Eur Acad Dermatol Venereol, 25 (2011) 130-137.

[46] F. Osei-Yeboah, Y. Feng, C.C. Sun, Evolution of structure and properties of granules containing microcrystalline cellulose and polyvinylpyrrolidone during high-shear wet granulation, J Pharm Sci, 103 (2014) 207-215.

[47] X. Kong, S. Zhang, Y. Wang, Y. Liu, R. Li, X. Ren, T.-S. Huang, Antibacterial polyvinyl alcohol films incorporated with N-halamine grafted oxidized microcrystalline cellulose, Composites Communications, 15 (2019) 25-29.

[48] H. Jafari, K.V. Bernaerts, G. Dodi, A. Shavandi, Chitooligosaccharides for wound healing biomaterials engineering, Mater Sci Eng C Mater Biol Appl, 117 (2020) 111266.

[49] P. Zou, J. Suo, L. Nie, S. Feng, Temperature-sensitive biodegradable mixed star-shaped block copolymers hydrogels for an injection application, Polymer, 53 (2012) 1245-1257.

[50] P. Zou, J. Suo, L. Nie, S. Feng, Temperature-responsive biodegradable star-shaped block copolymers for vaginal gels, Journal of Materials Chemistry, 22 (2012) 6316-6326.

[51] P. Makvandi, G.W. Ali, F. Della Sala, W.I. Abdel-Fattah, A. Borzacchiello, Biosynthesis and characterization of antibacterial thermosensitive hydrogels based on corn silk extract, hyaluronic acid and nanosilver for potential wound healing, Carbohydr Polym, 223 (2019) 115023.

[52] X. Yang, K. Yang, S. Wu, X. Chen, F. Yu, J. Li, M. Ma, Z. Zhu, Cytotoxicity and wound healing properties of PVA/ws-chitosan/glycerol hydrogels made by irradiation followed by freeze–thawing, Radiation Physics and Chemistry, 79 (2010) 606-611.

[53] L. Cai, X. Qin, Z. Xu, Y. Song, H. Jiang, Y. Wu, H. Ruan, J. Chen, Comparison of cytotoxicity evaluation of anticancer drugs between real-time cell analysis and CCK-8 method, Acs Omega, 4 (2019) 12036-12042.

[54] M. Avci, M. Heck, E.A. O'Rear, D.V. Papavassiliou, Hemolysis estimation in turbulent flow for the FDA critical path initiative centrifugal blood pump, Biomechanics and Modeling in Mechanobiology, 20 (2021) 1709-1722.

[55] J.H. Kim, Y.S. Shin, Effects of localized heating on pain, skin perfusion, and wound healing after lumbar decompression, Journal of Neuroscience Nursing, 52 (2020) 251-256.

[56] L. Nie, P. Zou, S. Feng, J. Suo, Temperature-sensitive star-shaped block copolymers hydrogels for an injection application: Phase transition behavior and biocompatibility, Journal of Materials Science: Materials in Medicine, 24 (2013) 689-700.

[57] G.C. Gurtner, S. Werner, Y. Barrandon, M.T. Longaker, Wound repair and regeneration, Nature, 453 (2008) 314-321.

[58] Z. Meng, H. Chen, S. Meng, The Roles of Tetramethylpyrazine During Neurodegenerative Disease, Neurotox Res, 39 (2021) 1665-1677.